Journal of Materials Chemistry C

ROYAL SOCIETY OF CHEMISTRY

PAPER

View Article Online
View Journal | View Issue

Check for updates

Cite this: J. Mater. Chem. C, 2023, 11, 3375

Near-infrared $Sr_7NaGa(PO_4)_6:Cr^{3+},Ln^{3+}$ (Ln = Nd, Er, and Yb) phosphors with different energy transfer paths: photoluminescence enhancement and versatility†

Chuansheng Zhong,[ab] Yonghui Xu,[ab] Xiudi Wu,[ab] Shuwen Yin,[a] Xibao Zhang,[ab] Liang Zhou *[abc] and Hongpeng You *[abc]

Received 26th December 2022,
Accepted 7th February 2023

DOI: 10.1039/d2tc05502c

rsc.li/materials-c

Near-infrared phosphors are of great interest due to their unique, versatile luminescence properties and exciting application prospects. Herein, a novel broadband emission NIR phosphor $Sr_7NaGa(PO_4)_6:Cr^{3+}$ was synthesized successfully, and photoluminescence properties of the phosphor were studied. When Ln^{3+} ions were co-doped, the photoluminescence was enhanced. Compared with $Sr_7NaGa(PO_4)_6$:0.15Cr^{3+}, the total emission intensity of $Sr_7NaGa(PO_4)_6$:0.15Cr^{3+},0.15Yb^{3+} increased to 172%, the IQE of $Sr_7NaGa(PO_4)_6$:0.15Cr^{3+},0.15Nd^{3+} increased from 22 to 72%, and the thermal quenching of $Sr_7NaGa(PO_4)_6$:0.15Cr^{3+},0.50Er^{3+} suppressed effectively. Highly efficient energy transfer paths are formed in the $Sr_7NaGa(PO_4)_6$:0.15Cr^{3+},Ln^{3+} phosphors because of the shorter distances between Cr^{3+} ions and Ln^{3+} ions in the $Sr_7NaGa(PO_4)_6$ host. The energy transfer efficiencies of $Cr^{3+} \rightarrow Ln^{3+}$ are greater than 70%. Finally, the investigations on night vision, solar cells, and ratiometric luminescent thermometers demonstrate that the as-prepared NIR phosphors have the potential for multifunctional applications.

Open Access Article. Published on 09 February 2023. Downloaded on 5/20/2025 11:15:26 PM. This article is licensed under a Creative Commons Attribution 3.0 Unported Licence.

1. Introduction

Near-infrared (NIR) phosphors with emission in the range of 700–1700 nm have drawn widespread attention because of their unique, versatile luminescent properties and exciting application prospects.[1–4] NIR phosphor-converted LEDs (NIR pc-LEDs) are expected to be the next generation NIR light source due to their small size, high conversion efficiency, long lifetime, and environmental friendliness.[5,6] The NIR pc-LEDs with broadband NIR emission can be employed in some areas such as non-destructive analysis and night vision.[7,8] And the NIR pc-LEDs in special ranges such as 720–740 nm and 650–950 nm (first biological window) can be used to facilitate plant growth, distinguish tumor tissues, and identify blood oxygen levels.[9–11] In addition to NIR pc-LEDs, NIR phosphors are also used as luminescent thermometers or light-conversion materials. The luminescent thermometers prepared using NIR phosphors at first and second (1000–1700 nm) biological windows pave the way for photodynamic thermal therapy for cancer.[12–15] Some NIR phosphors converting sunlight into NIR light at 900–1100 nm are added to c-Si solar cells to improve the solar energy conversion efficiency of c-Si solar cells.[16–18] These application prospects provide a huge impetus to develop novel highly efficient multifunctional NIR phosphors.

Inorganic NIR phosphors are composed of host materials and active ions. The active ions for NIR emission comprise rare earth ions and transition metal ions, such as Nd^{3+}, Yb^{3+}, Er^{3+}, and Cr^{3+}.[4,19–22] The Nd^{3+} and Yb^{3+} ions emit NIR light around 1000 nm corresponding to the $^4F_{3/2}$–$^4I_{9/2}$ and $^4F_{3/2}$–$^4I_{11/2}$ transitions of Nd^{3+} ions and the $^2F_{5/2}$–$^2F_{7/2}$ transitions of Yb^{3+} ions.[23,24] They show only a small amount of narrow-band absorption in visible light attributed to their spin-forbidden f–f transitions. In contrast, Cr^{3+} doped NIR phosphors show broadband absorption in visible light due to the spin-allowed d–d transition of the Cr^{3+} ion and exhibit good thermal stability and high quantum efficiency.[25] However, the 3d electrons of Cr^{3+} ions tend to couple to host lattices leading to a non-radiative transition, which has a negative effect on the luminescence properties of Cr^{3+} doped NIR phosphors.[26–28]

Ln^{3+} and Cr^{3+} ion co-doped NIR phosphors can combine the advantages of both the ions to reduce non-radiative transition, improve the performance of NIR phosphors and increase their application potential. At present, some NIR phosphors have been reported such as $Ca_3Sc_2Si_3O_{12}:Cr^{3+}$, $LiGaP_2O_7:Cr^{3+}$,

[a] State Key Laboratory of Rare Earth Resource Utilization, Changchun Institute of Applied Chemistry, Chinese Academy of Sciences, Changchun 130022, P. R. China. E-mail: zhoul@ciac.ac.cn, hpyou@ciac.ac.cn; Fax: +86 431 85698041
[b] University of Science and Technology of China, Hefei 230026, P. R. China
[c] Ganjiang Innovation Academy, Chinese Academy of Sciences, Ganzhou 341000, China

† Electronic supplementary information (ESI) available. See DOI: https://doi.org/10.1039/d2tc05502c

Open Access Article. Published on 09 February 2023. Downloaded on 5/20/2025 11:15:26 PM. This article is licensed under a Creative Commons Attribution 3.0 Unported Licence.

$Ca_2LuScAl_2Si_2O_{12}:Cr^{3+}$, $LaMgAl_{11}O_{19}:Cr^{3+},Nd^{3+}/Yb^{3+}$, $Ca_3Ga_2Ge_3O_{12}:Cr^{3+},Nd^{3+}$, $Ba_2LaGa_{11}O_{20}:Cr^{3+},/Nd^{3+}/Yb^{3+}$, $LaGaO_3:Cr^{3+},Yb^{3+}/Nd^{3+}/Er^{3+}$, $La_3LuGa_4O_{12}:Cr^{3+},Nd^{3+}$, and $LiScP_2O_7:Cr^{3+},Yb^{3+}$.[12,16,29–35] The $Sr_9Ga(PO_4)_7:Cr^{3+}$ and $Sr_9Cr(PO_4)_7:Yb^{3+}$ phosphors have been reported by Liu's work;[36,37] the work reported that the structure confinement of $Sr_9M(PO_4)_7$ (M = Ga and Cr) can enhance the luminescence properties of the NIR phosphors. In the $Sr_9Cr(PO_4)_7:Yb^{3+}$ phosphors, the energy transfer between Cr^{3+} and Yb^{3+} has been studied in detail. However, the energy transfer between Cr^{3+} and other rare earth ions such as Nd^{3+} and Er^{3+} has not been studied in this system, and the effect of the structure on different energy transfer paths and the application of phosphors co-doped with different rare earth ions need to be further investigated.

In this work, we report a novel NIR phosphor $Sr_7NaGa(PO_4)_6:Cr^{3+}$ (SNGP:Cr^{3+}) with a broadband emission (λ_{max} = 840 nm, FWHM = 140 nm) that can be effectively excited by the light from the commercial blue chip. More importantly, the PL properties including total emission intensity, internal quantum efficiency (IQE), and thermal stability of the SNGP:Cr^{3+} phosphors can be enhanced by co-doping Ln^{3+} (Yb^{3+}, Nd^{3+}, and Er^{3+}). The energy transfers from the Cr^{3+} to Ln^{3+} ions were studied in detail through analyzing the structure and radiation and non-radiation rates of Cr^{3+} ions, and decay rates of Ln^{3+} ions in the phosphors. We observed that some absorption energy of the Cr^{3+} ions is transferred to the Ln^{3+} ions, and the high energy transfer efficiencies of $Cr^{3+} \rightarrow Ln^{3+}$ (>70%) are attributed to the shorter distance between the Cr^{3+} ions and Ln^{3+} ions in the SNGP: Cr^{3+},Ln^{3+} phosphors. Furthermore, we explored the potential of the SNGP:Cr^{3+},Ln^{3+} phosphors for multifunctional applications.

2. Experimental section

2.1. Synthesis

$Sr_7NaGa(PO_4)_6:Cr^{3+},Yb^{3+}/Nd^{3+}/Er^{3+}$ NIR phosphors were synthesized using a traditional high temperature solid-state reaction. The raw materials, $SrCO_3$ (AR), Na_2CO_3 (AR), Ga_2O_3 (99.99%), $NH_4H_2PO_4$ (AR), Cr_2O_3 (AR), Yb_2O_3 (99.99%), Nd_2O_3 (99.99%), and Er_2O_3 (99.99%) were weighted according to stoichiometric amounts and grounded in an agate mortar for 20 min. Then, the mixtures were transferred to alumina crucibles and sintered at 1100 °C for 4 h in air. The final products were cooled to room temperature and reground to obtain homogeneous powders for analysis.

2.2. Characterization

X-ray diffraction (XRD) of the prepared samples was executed on a Bruker AXs D8 diffractometer with Cu Kα X-radiation at 40 kV, 40 mA and λ = 0.15405 nm. Energy-dispersive X-ray spectroscopy (EDS) elemental mappings were carried out using a Hitachi-S4800 system (Japan). The photoluminescence (PL) and photoluminescence excitation (PLE) spectra were recorded using an Edinburgh FLSP-920 fluorescence spectrophotometer equipped with a 450 W Xe lamp. The decay curves were collected using the same spectrophotometer with a μF900 flash lamp. A series of temperature dependent PL spectra from 298 to 423 K were recorded on a FLSP-920 system with a temperature controller.

2.3. NIR pc-LED fabrication and performance measurement

The as-prepared NIR phosphors were first mixed with epoxy resins and then coated on 460 nm chips. The mixtures were cured at 120 °C for 1 h to form the final LED devices. The electroluminescence performance was measured using a HAAS 2000 photoelectric measuring system from EVERFINE.

3. Results and discussion

3.1. Phase and structural analysis

Fig. 1a depicts the crystal structure of SNGP, and there are four different Sr sites, Sr1, Sr2, Sr3, and Sr4, in the structure. The Sr1, Sr2, Sr3, and Sr4 sites are surrounded by nine, eight, and seven oxygen atoms forming polyhedra, respectively. Ga connects six oxygen atoms forming [GaO_6] octahedra. Due to the similar radii and charges of Cr^{3+} ions (r = 0.615 Å, CN = 6) and Ga^{3+} ions (r = 0.620 Å, CN = 6), Cr^{3+} ions prefer to substitute Ga^{3+} ions. While Ln^{3+} ions tend to replace Sr^{2+} ions because the radius of Ln^{3+} ions is much larger than that of Ga^{3+} ions but similar to that of Sr^{2+} ions. Notably, the distances between adjacent Ga^{3+} ions are large ranging from 8.984 to 17.968 Å, and the distances between Ga^{3+} ions and Sr^{2+} ions are short ranging from 3.687 to 5.314 Å. The XRD patterns of SNGP:$x$$Cr^{3+}$ (x = 0.10, 0.15, 0.30, 0.50, 0.70, and 0.90) were obtained to verify the phase purity. Fig. 1b shows that all diffraction peaks of samples match well with the standard card of $Sr_9Ga(PO_4)_7$ (PDF # 53-0180). The result indicates that the pure phase samples have been prepared successfully. With an increase in Cr^{3+}-concentration, the diffraction peaks of SNGP:$x$$Cr^{3+}$ shift to a higher angle region (Fig. 1b), which is caused by lattice expansion due to the large Ga^{3+} ions being replaced with smaller Cr^{3+} ions. The result means that smaller Cr^{3+} ions dissolve into the SNGP host and reduce the lattice space. Fig. S1 (ESI†) displays the XRD patterns of SNGP:Cr^{3+},Ln^{3+} phosphors, and no other peaks except pure phase peaks are observed.

Fig. 1c illustrates the calculated and experimental diffractograms of SNGP:0.15Cr^{3+} phosphors obtained from XRD Rietveld refinement. Table 1 represents mainly the results of the refined crystal structure, where the lower R factor of the sample ensures the accuracy of the refinement. These results confirm that SNGP:Cr^{3+} possesses a monoclinic structure with space group $I2/a1$. Moreover, Fig. 2 shows the elemental mapping images of SNGP:0.30Cr^{3+}, where the constituent elements Sr, Na, Ga, P, O, and Cr are well distributed within the hole particle, meaning that Cr^{3+} ions have been successfully introduced into the host.

3.2. Luminescence properties of SNGP:Cr^{3+} phosphors

Fig. 3a illustrates the PL and PLE spectra of SNGP:0.15Cr^{3+}. The PLE spectrum monitored at 840 nm exhibits two absorption bands centered at 487 and 704 nm, originating from the $^4A_{2g} \rightarrow {}^4T_{1g}$ and $^4A_{2g} \rightarrow {}^4T_{2g}$ transitions of Cr^{3+} ions. The effective

 This journal is © The Royal Society of Chemistry 2023

Open Access Article. Published on 09 February 2023. Downloaded on 5/20/2025 11:15:26 PM.
This article is licensed under a Creative Commons Attribution 3.0 Unported Licence.

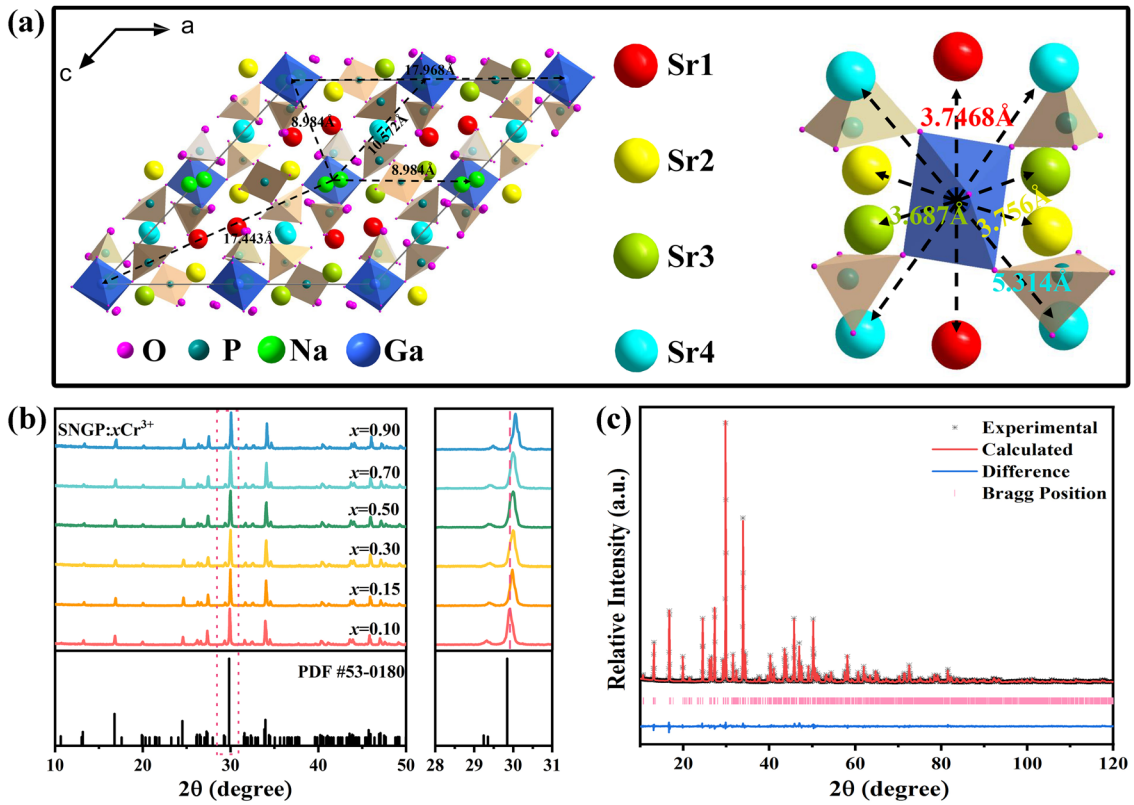

Fig. 1 (a) Crystal structure of the SNGP host; distances between adjacent Ga^{3+} ions, and distances between Ga^{3+} ions and Sr^{2+} ions. (b) XRD patterns of SNGP:xCr^{3+} (x = 0.10, 0.15, 0.30, 0.50, 0.70, and 0.90) (c) Rietveld refinement of SNGP:0.15Cr^{3+} phosphors.

excitation band is close to 460 nm, matching well with the emission of the commercial blue chip, and has application prospects in NIR pc-LED production. The PL spectrum shows a broadband emission peaking at 840 nm and a full width at half maximum (FWHM) of 140 nm (Fig. 3a). There is a strong relationship between crystal field strength of the host and Cr^{3+} emission. In general, when D_q/B is greater than 2.3, the host is considered to have a strong crystal field, and Cr^{3+} ions show a narrow-band emission around 700 nm; when D_q/B is less than 2.3, the host has a weak crystal field, and Cr^{3+} ions produce a broadband emission. The crystal field strength of SNGP:0.15Cr^{3+} was calculated using the following equations:[11]

$$D_q = \frac{E(^4A_{2g} \rightarrow {}^4T_{2g}) - \Delta S/2}{10} \quad (1)$$

$$x = \frac{E(^4A_{2g} \rightarrow {}^4T_{1g}) - E(^4A_{2g} \rightarrow {}^4T_{2g})}{D_q} \quad (2)$$

$$\frac{D_q}{B} = \frac{15(x-8)}{(x^2-10x)} \quad (3)$$

where $E(^4A_{2g}$–$^4T_{2g})$ and $E(^4A_{2g}$–$^4T_{1g})$ relate to the transition energy of $^4A_{2g}$–$^4T_{2g}$ and $^4A_{2g}$–$^4T_{1g}$ corresponding to the energy position of the excitation band, and ΔS is the Stokes shift. The D_q/B value of sample was determined to be 1.93, revealing that the Cr^{3+} ions are located in a weak crystal field environment. Fig. 3b depicts the Tanabe–Sugano diagram for the Cr^{3+} ions in an octahedral crystal field environment, where the $^4A_{2g} \rightarrow {}^4T_{2g}$ transition is the dominant transition as D_q/B is less than 2.3. It proves that the broadband emission of samples originates from the $^4A_{2g} \rightarrow {}^4T_{2g}$ transition in a weak crystal field environment. Fig. 3c plots the PL spectra of SNGP:xCr^{3+} (x = 0.10, 0.15, 0.30, 0.50, 0.70, and 0.90). As Cr^{3+}-concentration increases, the emission intensity of samples first increases and then decreases, and the emission intensity is maximum at x = 0.15. The phenomenon is concentration quenching caused by energy transfer between adjacent Cr^{3+} ions. From the structural analysis above, the distances (8.984 to 17.968 Å) between

Table 1 Refined crystal structure results of the SNGP:0.15Cr^{3+} phosphor

Compound	SNGP:0.15Cr^{3+}
Space group	$I2/a1$
a/Å	17.96
b/Å	10.56
c/Å	18.30
v/Å^3	3102.8
$\alpha = \beta$/deg	90
γ/deg	133
Z	4
2θ/deg	10–120
R_{wp}, %	0.0849
R_P, %	0.0594
χ^2	6.7

Open Access Article. Published on 09 February 2023. Downloaded on 5/20/2025 11:15:26 PM.
This article is licensed under a Creative Commons Attribution 3.0 Unported Licence.

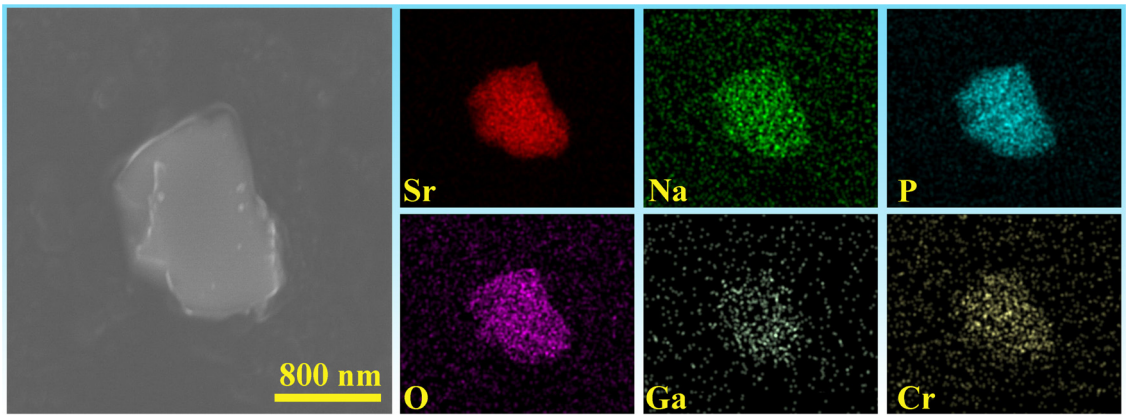

Fig. 2 SEM image and elemental maps of the SNGP:0.30Cr^{3+} phosphor.

adjacent Cr^{3+} ions exceed the exchange interaction distance (~5 Å) because of Ga^{3+} ions being replaced with Cr^{3+}. Thus, the energy transfer mechanism between adjacent Cr^{3+} ions in the host is electric multipolar interaction rather than exchange interaction. The concentration quenching was further studied through the relationship between concentration and intensity of SNGP:$x$$Cr^{3+}$ (Note S1, ESI†) and we found that the multipolar interaction belongs to dipole–dipole (d–d) interactions. As the Cr^{3+}-concentration increases, the multipolar interaction strengthens, leading to a nonradiative transition enhancement and concentration quenching. Concentration-induced nonradiative transition can be demonstrated using decay curves.

As shown in Fig. 3d, all decay curves are fitted with a single exponential function, meaning that there is only one site for Cr^{3+} to occupy in the host. The lifetimes of samples decrease with an increase in Cr^{3+}-concentration, which can be explained using the formula given below:[38,39]

$$\frac{1}{\tau} = \frac{1}{\tau_0} + A_{nr} + P_t \quad (4)$$

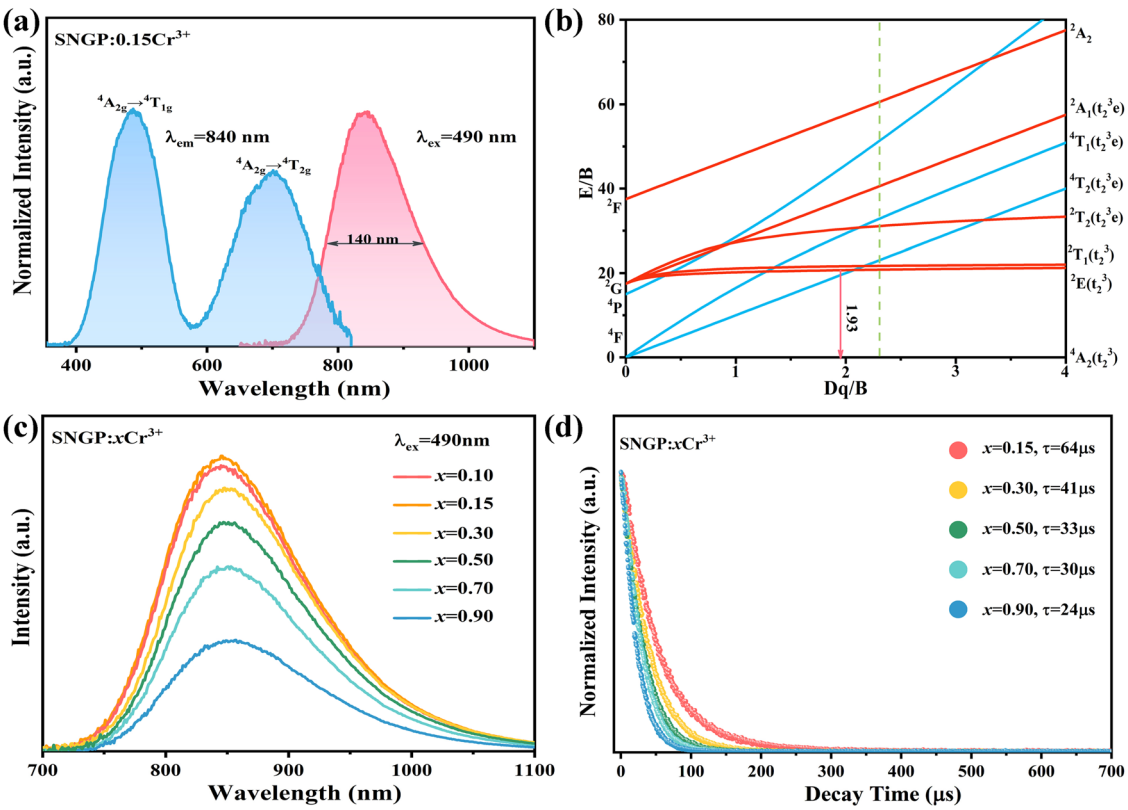

Fig. 3 (a) PLE and PL spectra of SNGP:0.15Cr^{3+}. (b) Tanabe–Sugano diagram for Cr^{3+} in an octahedral crystal field environment. (c) Relationship between concentration and emission intensity of the Cr^{3+} ions in SNGP:$x$$Cr^{3+}$ (x = 0.10, 0.15, 0.30, 0.50, 0.70, and 0.90). (d) Decay curves of SNGP:$x$$Cr^{3+}$ (x = 0.15, 0.30, 0.50, 0.70, and 0.90).

 This journal is © The Royal Society of Chemistry 2023

Open Access Article. Published on 09 February 2023. Downloaded on 5/20/2025 11:15:26 PM.
This article is licensed under a Creative Commons Attribution 3.0 Unported Licence.

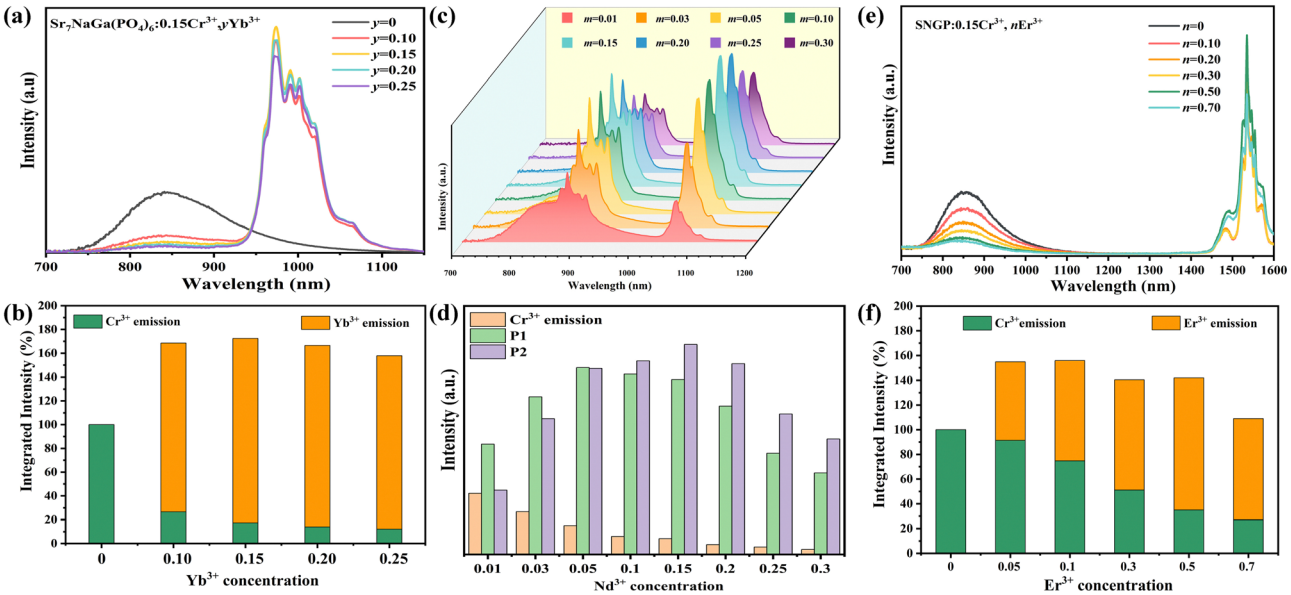

Fig. 4 (a) PL spectra of SNGP:0.15Cr^{3+},yYb^{3+} (y = 0, 0.10, 0.15, 0.20, and 0.25) (b) integrated intensities of the total emission, Cr^{3+}-emission, and Yb^{3+}-emission in SNGP:0.15Cr^{3+},yYb^{3+} phosphors with various Yb^{3+}-concentrations. The total emission is the sum of the Cr^{3+}-emission and Yb^{3+}-emission. (c) PL spectra of SNGP:0.15Cr^{3+},mNd^{3+} (m = 0.01, 0.03, 0.05, 0.10, 0.15, 0.20, 0.25, and 0.30). (d) Relative intensities of P1, P2 and Cr^{3+}-emission in SNGP:0.15Cr^{3+},mNd^{3+} phosphors. (e) PL spectra of SNGP:0.15Cr^{3+},nEr^{3+} (n = 0, 0.05, 0.10, 0.30, 0.50, and 0.70). (f) Integrated intensities of the total emission, Cr^{3+}-emission, and Er^{3+}-emission in SNGP:0.15Cr^{3+},nEr^{3+} phosphors with various Er^{3+}-concentrations.

where τ_0 stands for the radiative lifetime, A_{nr} and P_t represents the nonradiative rate depending on multiphonon relaxation and the energy transfer rate. On the basis of the equation, we know that the nonradiative rate increases with an increase in Cr^{3+}-concentration, leading to an attenuation of the lifetimes. The result demonstrates that concentration induces a nonradiative transition that not only has a negative effect on the luminescence intensity, but also reduces the thermal stability and quantum efficiency of phosphors. In addition to concentration variation, the nonradiative transition can be caused by other factors such as temperature and defects. The PL spectra of SNGP:0.15Cr^{3+} (phosphor **1**) at different temperatures (Fig. S2, ESI†) and IQE of the phosphor were measured. The thermal stability of phosphor **1** is poor and the IQE is only about 22%. Therefore, it is necessary that the PL properties of SNGP:Cr^{3+} are further improved by inhibiting the nonradiative transition of the phosphor.

3.3. PL enhancement through the energy transfer paths of SNGP:Cr^{3+},Ln^{3+}

Fig. 4a, c and e displays the PL spectra of SNGP:0.15Cr^{3+},yYb^{3+} (y = 0, 0.10, 0.15, 0.20, and 0.25), SNGP:0.15Cr^{3+},mNd^{3+} (m = 0.01, 0.03, 0.05, 0.10, 0.15, 0.20, 0.25, and 0.30), and SNGP:0.15Cr^{3+},nEr^{3+} (n = 0, 0.05, 0.1, 0.3, 0.5, and 0.7), respectively. The spectra of SNGP:0.15Cr^{3+},yYb^{3+} (y = 0.10, 0.15, 0.20, and 0.25) ranging from 700 to 1100 nm show the characteristic emission of both Cr^{3+} ions and Yb^{3+} ions. With an increase in Yb^{3+}-concentration, the emission intensity of the Cr^{3+} ions decreases, while that of Yb^{3+} ions increases and reaches the maximum when y = 0.15. The result indicates that the energy of some Cr^{3+} ions is transferred to Yb^{3+} ions in SNGP:0.15Cr^{3+},yYb^{3+}. The total emission intensity of SNGP:0.15Cr^{3+},0.15Yb^{3+} (phosphor **2**) increases to 172% (Fig. 4b), compared with that of phosphor **1**. Similarly, the spectra of SNGP:0.15Cr^{3+},mNd^{3+} show the emission of Cr^{3+} ions and Nd^{3+} ions, and the emission intensity of the Nd^{3+} ions reaches the maximum with m = 0.10. In addition, the emission spectrum of the Nd^{3+} ions is composed of two peaks at 877 (P1) and 1060 nm (P2), corresponding to the $^4F_{3/2} \rightarrow {}^4I_{9/2}$ and $^4F_{3/2} \rightarrow {}^4I_{11/2}$ transitions of the Nd^{3+} ions, respectively, and a regular variation in the relative intensities of two peaks depends on Nd^{3+}-concentration. As depicted in Fig. 4d, the emission intensity of P1 is higher than that of P2, when m is less than 0.05, while the emission intensity of P2 is higher than that of P1 when m exceeds 0.05. The interesting phenomenon can be explained by emission spectral overlap of the Cr^{3+} ions and the Nd^{3+} ions. Initially, the emission intensity of P1 is higher than that of P2 because the emission intensity of Cr^{3+} is high. However, with increasing Nd^{3+}-concentration, the emission intensity of Cr^{3+} ions decreases because of the energy transfer from Cr^{3+} to Nd^{3+} ions. As a result, the intensity of P1 gradually decreases to less than the intensity of P2. As shown in Fig. S3 (ESI†), the total emission intensity of SNGP:0.15Cr^{3+},0.1Nd^{3+} (phosphor **3**) increases to 113%. For SNGP:0.15Cr^{3+},nEr^{3+}, the energy transfer from Cr^{3+} to Er^{3+} ions is observed in Fig. 4e, and the total emission intensity of SNGP:0.15Cr^{3+},0.5Er^{3+} (phosphor **4**) increases to 156% in comparison with phosphor **1** (Fig. 4f). These results reveal that the enhancement of total emission intensity is caused by $Cr^{3+} \rightarrow Ln^{3+}$ energy transfer. The energy transfer mechanisms are revealed by the energy transfer scheme given in Fig. 5. The electrons of the Cr^{3+} ions are pumped from the ground state $^4A_{2g}$ to excited states $^4T_{1g}$, and $^4T_{2g}$ after absorbing 490 and 704 nm light, respectively. Then the electrons relax to the $^4T_{2g}$ state and transfer some energy to the Yb^{3+} ions/ Nd^{3+} ions/ Er^{3+} ions, leading to the pumping of electrons

Open Access Article. Published on 09 February 2023. Downloaded on 5/20/2025 11:15:26 PM.
This article is licensed under a Creative Commons Attribution 3.0 Unported Licence.

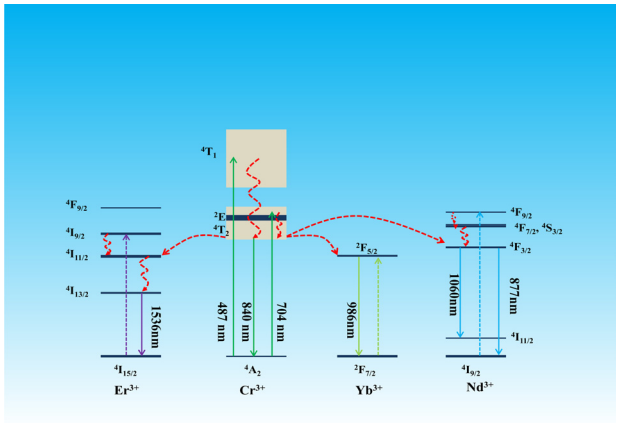

Fig. 5 Energy transfer mechanisms of Cr^{3+} → Ln^{3+} in the SNGP:0.15Cr^{3+},Ln^{3+} phosphors.

of Yb^{3+} ions/the Nd^{3+} ions/the Er^{3+} ions from the ground state to the $^2F_{5/2}$ state of Yb^{3+} ions/the $^4F_{3/2}$ state of the Nd^{3+} ions/the $^4I_{11/2}$ state of the Er^{3+} ions. The electrons in the excited state of the Ln^{3+} ions come to the lower excited state *via* nonradiative transition, and finally return to the ground state to produce NIR emission.

The decay curves of the Cr^{3+} ions in SNGP:0.15Cr^{3+},Ln^{3+} (λ_{ex} = 490 nm, λ_{em} = 840 nm) with different Ln^{3+}-concentrations are plotted in Fig. 6a and Fig. S4a, b (ESI†). Due to Cr^{3+} → Ln^{3+} energy transfer, the lifetimes of Cr^{3+} in SNGP:Cr^{3+},Ln^{3+} decrease rapidly and the decay curves deviate from the single exponential rule. To better understand the energy transfer from the Cr^{3+} to Ln^{3+} ions, the average lifetime can be calculated using the equation as follows:[21,40]

$$\tau_{ave} = \frac{\int_0^\infty tI(t)\mathrm{d}t}{\int_0^\infty I(t)\mathrm{d}t} \quad (5)$$

The lifetimes of the Cr^{3+} ions in SNGP:0.15Cr^{3+},Ln^{3+}decrease continuously with increasing Ln^{3+}-concentration, confirming that the energy is transferred from Cr^{3+} to Ln^{3+} ions. The energy transfer efficiency (η) was calculated using the following equation:[41]

$$\eta = 1 - \frac{\tau}{\tau_0} \quad (6)$$

where τ and τ_0 are the lifetimes of Cr^{3+} ions in the presence and absence of Ln^{3+} ions, respectively. As shown in Fig. 6b and Fig. S4c, d (ESI†), the η value is determined to be 72%, 73% and 75% corresponding to SNGP:0.15Cr^{3+},0.30Nd^{3+}, SNGP:0.15Cr^{3+},0.70Er^{3+} and SNGP:0.15Cr^{3+},0.25Yb^{3+}, respectively. The high energy transfer efficiencies of Cr^{3+} → Ln^{3+} are attributed to the structure of SNGP:0.15Cr^{3+},Ln^{3+}. On the basis of the structural analysis above, the distances between the Cr^{3+} ions and Ln^{3+} ions are much shorter than those between adjacent Cr^{3+} ions because Ln^{3+} ions replace Sr^{2+} ions in the SNGP host. As a result, a compact Cr^{3+}–Ln^{3+} pair is formed in the host and a highly efficient Cr^{3+} → Ln^{3+} energy transfer is realized. Nd^{3+} usually connects eight or nine oxygen atoms, while Er^{3+} and Yb^{3+} can connect seven, eight or nine oxygen atoms. Thus, Nd^{3+} can substitute Sr1 and Sr2 in SNGP:Cr^{3+},Nd^{3+}, but Er^{3+} and Yb^{3+} can substitute Sr1, Sr2, Sr3 and Sr4 in SNGP:Cr^{3+},Er^{3+} and SNGP:Cr^{3+},Yb^{3+}, respectively. According to the Dexter theory, the shorter the distance between the sensitizer and activator, the higher the energy transfer efficiency. The refined distances between Cr^{3+} and Ln^{3+} corresponding to SNGP:0.15Cr^{3+},0.30Nd^{3+}, SNGP:0.15Cr^{3+},0.70Er^{3+} and SNGP:0.15Cr^{3+},0.25Yb^{3+} are listed in Table S1 (ESI†). The average refined distance of Yb and Cr is shorter than that of the other two. The result means that the Cr^{3+} → Yb^{3+} energy transfer is the most efficient in SNGP:0.15Cr^{3+},Ln^{3+}, which is consistent with the above experimental result.

Moreover, the Cr^{3+} → Ln^{3+} energy transfer paths were analyzed in detail through the ET efficiency (η), radiative (W_R) rates, and nonradiative (W_{NR}) transition rates, which can be expressed using the following eqn (7)–(12):[30]

$$\eta = \frac{W_{ET}}{W_{ET} + W_R + W_{NR}} \quad (7)$$

$$IQE_0 = \frac{W_R}{W_R + W_{NR}} \quad (8)$$

$$\frac{1}{\tau} = W_{ET} + W_R + W_{NR} \quad (9)$$

$$\frac{1}{\tau_0} = W_R + W_{NR} \quad (10)$$

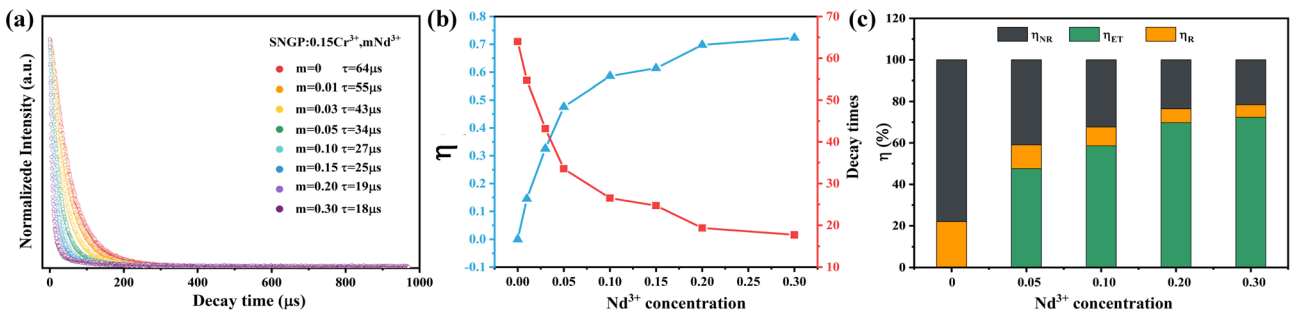

Fig. 6 (a) Decay curves of Cr^{3+} ions in SNGP:0.15Cr^{3+},mNd^{3+} (*m* = 0, 0.01, 0.03, 0.05, 0.10, 0.15, 0.20, and 0.30). (b) Energy transfer efficiency (η) of Cr → Nd^{3+} and lifetimes of Cr^{3+} in the SNGP:0.15Cr^{3+},mNd^{3+} phosphors at different Nd^{3+} concentrations. (c) Values of η_{ET}, η_R, and η_{NR} at various Nd^{3+} concentrations.

 This journal is © The Royal Society of Chemistry 2023

Open Access Article. Published on 09 February 2023. Downloaded on 5/20/2025 11:15:26 PM.
This article is licensed under a Creative Commons Attribution 3.0 Unported Licence.

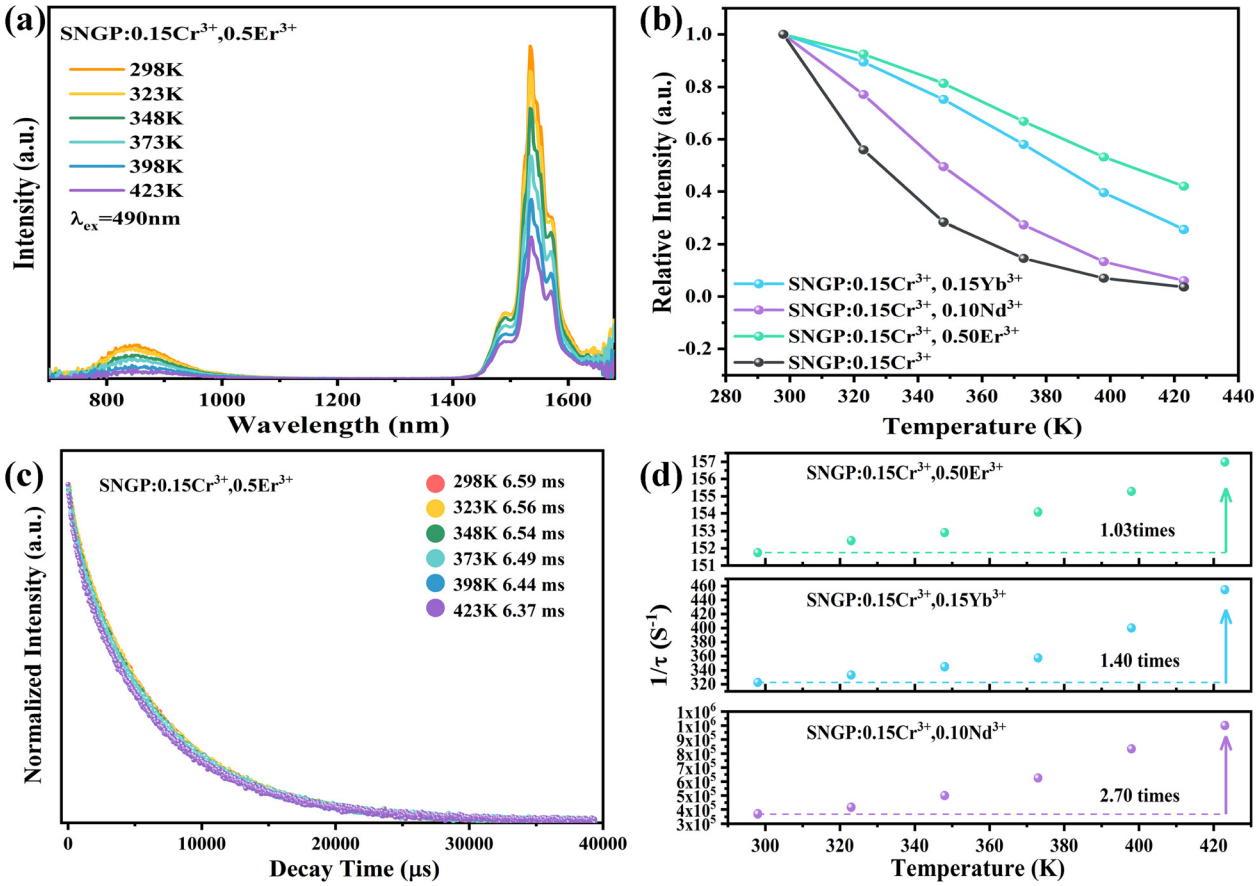

Fig. 7 (a) PL spectra of phosphor **4** at different temperatures. (b) Dependencies of PL intensities for phosphors **1–4** on temperature. (c) Decay curves of phosphor **4** at different temperatures. (d) Decay rates ($1/\tau$) of the Nd^{3+}, Yb^{3+} and Er^{3+} luminescence at different temperatures corresponding to phosphors **2–4**.

According to eqn (6)–(10), the W_R and W_{NR} are defined as

$$\eta_R = \frac{W_R}{W_{ET} + W_R + W_{NR}} \quad (11)$$

$$\eta_{NR} = \frac{W_{NR}}{W_{ET} + W_R + W_{NR}} \quad (12)$$

The η, η_R, and η_{NR} values were calculated using eqn (6)–(12). The values are plotted in Fig. 6c and Fig. S4e, f (ESI†), and the ratio of radiative and nonradiative transition rates reduces as Ln^{3+}-concentration increases. When Ln^{3+} ions are co-doped, part of absorption energy for both radiative and nonradiative transitions of Cr^{3+} ions is transferred to the Ln^{3+} ions, which means that the nonradiative transition of the Cr^{3+} ions is suppressed. As a result, the IQE and thermal stability of phosphor **1** are enhanced by co-doping Ln^{3+} ions. The IQEs of phosphors **2–4** were measured to be 70.6, 72.8, and 49.3%, respectively (Note S2, ESI†).

The PL spectra of phosphors **2–4** at different temperatures from 298 to 423 K are shown in Fig. S5a, b and Fig. 7a (ESI†), respectively. The relationships between the emission intensities of phosphors **2–4** and temperatures are plotted in Fig. 7b. Obviously, the thermal quenching is evidently reduced by co-doping Er^{3+} and Yb^{3+} ions. For instance, ~56 and 75% of the original integral intensity can be retained at 100 °C for phosphors **2** and **3**, respectively (~16%@100 °C for SNGP:0.15Cr^{3+}). However, there is basically no change in thermal stability of phosphor **3**, compared with phosphors **1**. According to a previous report, Yb^{3+} and Er^{3+} have the ability to replace a small amount of Ga^{3+}, while the larger Nd^{3+} ions can only occupy Sr^{2+} sites.[42] Thus, SNGP:Cr^{3+},Nd^{3+} phosphors have far more charge defects than SNGP:Cr^{3+},Yb^{3+} and SNGP:Cr^{3+},Er^{3+} phosphors. Although the IQE of phosphor **3** is the highest, the phosphor shows more non-radiative transitions due to the charge defects. Therefore, there is no significant improvement in thermal stability of phosphor **3**. The non-radiative transitions of phosphors **2–4** were studied using temperature-dependent decay curves (Fig. S5c, d and Fig. 7c, ESI†). The lifetimes of the Ln^{3+} ions decrease as the temperature increases, and their decay rates ($1/\tau$) are plotted in Fig. 7d as a function of temperature. All the decay rates of Ln^{3+} ions increase with increasing temperature because the rate of thermally activated nonradiative transition increases, and the decay rate of Nd^{3+} is highest and that of Er^{3+} is the lowest. Compared with phosphor **3**, the nonradiative transitions of phosphors **2** and **4** are better suppressed to enhance the thermal stability of phosphor **1**, promoting its application potential that will be explored in detail in the next section.

Open Access Article. Published on 09 February 2023. Downloaded on 5/20/2025 11:15:26 PM.
This article is licensed under a Creative Commons Attribution 3.0 Unported Licence.

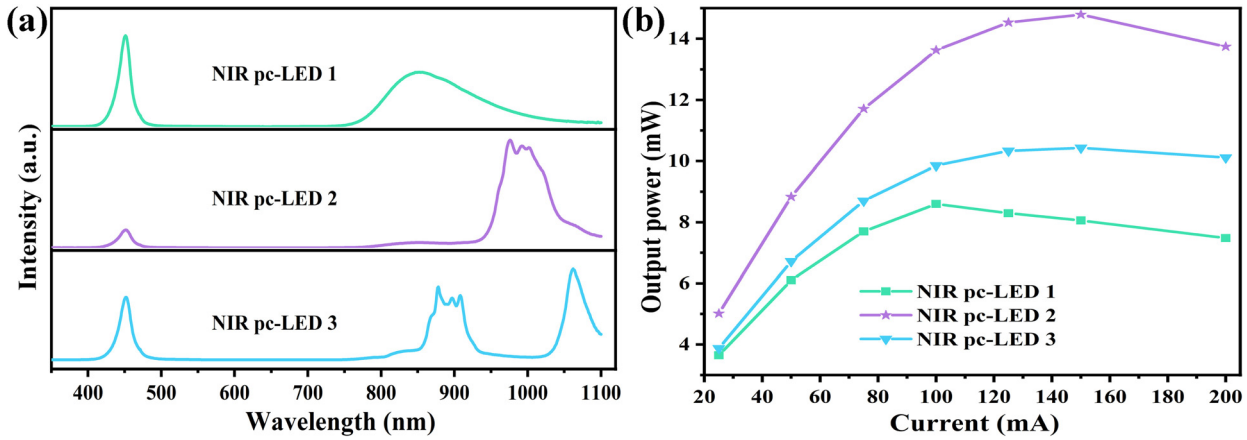

Fig. 8 (a) Electroluminescence spectra of NIR pc-LED 1–3 at 20 mA drive current. (b) Output powers of NIR pc-LED 1–3 at different drive currents.

4. Multifunctional application of SNGP:Cr^{3+},Ln^{3+} phosphors

4.1. Applications in NIR pc-LEDs

The NIR pc-LEDs 1–3 were prepared by coating phosphors **1–3** on blue chips (λ_{em} = 450 nm), respectively, and the NIR pc-LEDs 1–3 are effectively excited using blue chips and exhibit NIR emissions (Fig. 8a). Fig. S6a–c (ESI†) shows their electroluminescence spectra at different driving currents. As detailed in Fig. 8b, the output powers of the NIR pc-LEDs due to the saturated effect first increase and then fall with increasing current. The application of NIR pc-LEDs for night vision was designed and tested. Fig. 9 shows the fruit images obtained under natural light and NIR pc-LED 2. The fruit image is clear and shows the conventional color under natural light, and nothing can be captured when the natural light is tuned off. When NIR pc-LED 3 is turned on, the fruit image is captured clearly using a 760 nm filter. Compared with NIR pc-LED 1, the fruit images under NIR pc-LEDs 2 and 3 are clearer due to their higher output powers (Fig. S7, ESI†). These results illustrate that phosphors **1–3** have a promising application in night vision. Then the penetrating abilities of NIR pc-LEDs 1–3 were tested. As shown in Fig. S7 (ESI†), the veins in the finger can be clearly observed under NIR pc-LEDs 1–3, indicating that phosphors **1–3** possess good penetrating abilities for application in tissue penetration.

4.2. Applications of c-Si based solar cells

Fig. 10 represents the AM 1.5 solar spectrum, the spectral response of c-Si solar cells, and the PLE and PL spectra of phosphors **2** and **3**. The PLE spectrum of phosphor **2** is consistent with the maximum photon flux region of the solar spectrum, and the PL spectrum matches well with the spectral response of c-Si solar cells. For phosphor **2**, the PLE spectrum comprises more absorption bands distributed in the UV-visible region of the solar spectrum. Its PL spectrum consisting of two emission bands matches well with the spectral response of c-Si solar cells, especially, the P2 is coherent with the region of maximum response. Therefore, phosphors **2** and **3** possess a substantial application potential in c-Si solar cells.

4.3. Application in ratiometric luminescent thermometers

The SNGP:0.15Cr^{3+},0.03Nd^{3+},0.15Er^{3+} phosphor was designed as a ratiometric luminescent thermometer for investigation. Fig. S8 (ESI†) shows the PL spectra of SNGP:0.15Cr^{3+},0.03Nd^{3+},0.15Er^{3+} from 173 to 423 K, and the emission intensities of both Nd^{3+} and Er^{3+} ions decrease at different rates when the temperature increases. As shown in Fig. 11a, the emission intensity of Nd^{3+} ions attenuates faster than that of Er^{3+} ions. The thermometric property of the sample was further evaluated from the luminescence intensity ratio (LIR) and relative sensitivity (S_R), which are two important parameters for thermometers. The LIR 1 (between P1 and Er^{3+}-emission) and LIR 2 (between P2 and Er^{3+}-emission) were calculated using the following equation:[43–46]

$$\mathrm{LIR} = \frac{I_{high}}{I_{low}} = \frac{\int I(Er^{3+})d\lambda}{\int I(Nd^{3+})d\lambda} = A\exp\left(\frac{-B}{T}\right) + C \qquad (13)$$

where I_{high} and I_{low} present the integral intensities of the

Fig. 9 Images of fruits illuminated with natural light and the NIR pc-LED 2 light.

 This journal is © The Royal Society of Chemistry 2023

Open Access Article. Published on 09 February 2023. Downloaded on 5/20/2025 11:15:26 PM.
This article is licensed under a Creative Commons Attribution 3.0 Unported Licence.

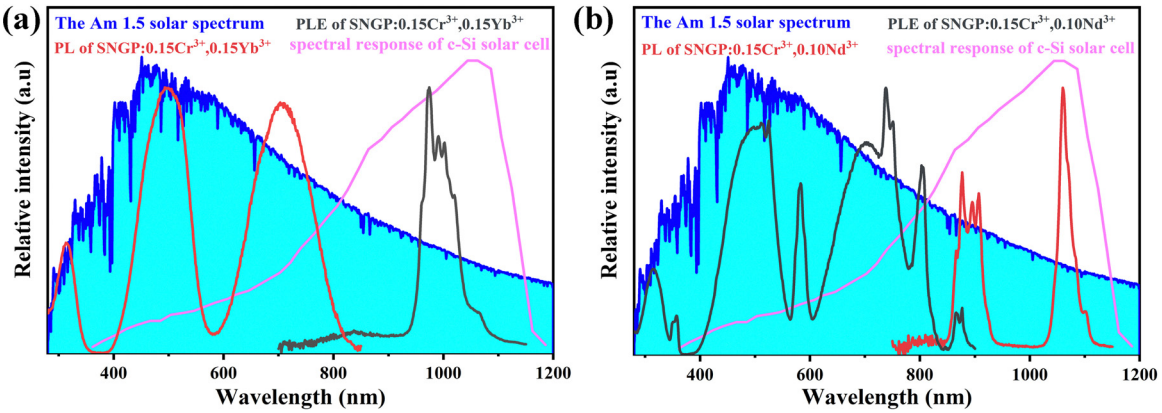

Fig. 10 AM 1.5 solar spectrum, the spectral response of c-Si solar cells, and the PLE and PL spectra of phosphors **2** and **3**.

high-energy emission band and low-energy emission band, respectively. A, B and C are constants. Fig. 11b and c shows the LIR 1 and LIR 2 at various $1/T$ values. Both LIR 1 and LIR 2 curves exhibit a slow decline from $1/T$ = 0.00562 K^{-1} (T = 178 K) to $1/T$ = 0.00366 K^{-1} (T = 273 K) and a fast decline from $1/T$ = 0.00366 K^{-1} (273 K) to $1/T$ = 0.00236 K^{-1} (423 K). The values of LIR 1 and LIR 2 at 423 K are 0.43 and 0.60, respectively. Then the S_{R1} of P1 and Er^{3+}-emission, and S_{R2} of P2 and Er^{3+}-emission were calculated using the following equations:[43–46]

$$S_R = \frac{1}{\mathrm{LIR}}\frac{\Delta \mathrm{LIR}}{\Delta T} \times 100\% = \frac{A\exp\left(\frac{-B}{T}\right)}{A\exp\left(\frac{-B}{T}\right)+C}\frac{B}{T^2} \times 100\% \quad (14)$$

where A, B and C are constants, and ΔLIR represents its change for ΔT change in temperature. The values of A, B, and C for S_{R1} are 553, −2624.7, and 0.46, respectively; the values of A, B, and C

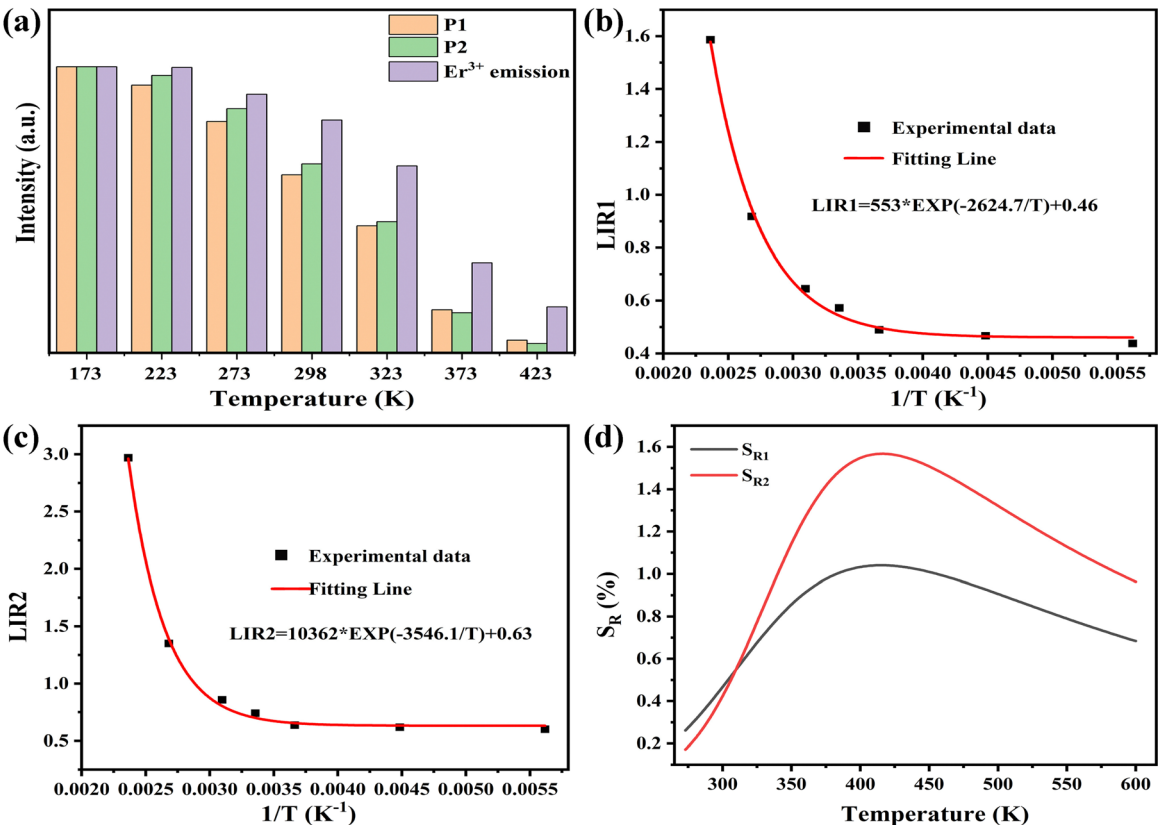

Fig. 11 (a) Histogram of the temperature-dependent emission intensity for P1, P2 and Er^{3+}-emission. (b) LIR 1 *versus* $1/T$ (c) LIR 2 *versus* $1/T$. (d) Dependencies of S_{R1} and S_{R2} on temperature.

Open Access Article. Published on 09 February 2023. Downloaded on 5/20/2025 11:15:26 PM.
This article is licensed under a Creative Commons Attribution 3.0 Unported Licence.

for S_{R2} are 10 362, −3456.1, and 0.632, respectively. These values are obtained by fitting the experimental LIR 1 and LIR 2 data points in Fig. 11b and c. Fig. 11d plots the S_{R1} and S_{R2} at different temperatures. It is observed that both S_{R1} and S_{R2} increase and then decrease with increasing temperature. When $T > 309$ K, S_{R2} is significantly higher than S_{R1}, and the value of S_{R2} is greater than 1% in the range from 340 to 588 K. The result means that the relative emission intensity of P2 and Er^{3+} emission is more suitable for ratiometric luminescent thermometers and indicates that SNGP:0.15Cr^{3+},0.03Nd^{3+},0.15Er^{3+} is a good candidate for ratiometric luminescent thermometers.

5. Conclusion

In this work, a novel NIR phosphor SNGP:Cr^{3+} was synthesized using a solid state reaction method, and the phosphor exhibits a broadband emission peak at 849 nm with a FWHM of 140 nm. When Ln^{3+} ions were co-doped into SNGP:0.15Cr^{3+} phosphors, different $Cr^{3+} \rightarrow Ln^{3+}$ energy transfer paths were formed which enhanced the PL properties of the phosphors. The total emission intensity of SNGP:0.15Cr^{3+},0.15Yb^{3+} increased to 172%, the IQE of SNGP:0.15Cr^{3+},0.15Yb^{3+}/0.10Nd^{3+} is greater than 70%, and the thermal quenching of SNGP:Cr^{3+} is obviously inhibited by co-doping Er^{3+} ions. More importantly, the $Cr^{3+} \rightarrow Ln^{3+}$ energy transfer paths were further investigated. We found that the high energy transfer efficiency is attributed to the shorter distances between Cr^{3+} ions and Ln^{3+} ions; both radiative and nonradiative absorption energies of Cr^{3+} ions are transferred to Ln^{3+} ions. The energy transfer efficiency of $Cr^{3+} \rightarrow Yb^{3+}$ is the highest, reaching 75%, and co-doping with Yb^{3+} ions or Er^{3+} ions better suppress the temperature induced nonradiative transition of the SNGP:Cr^{3+} phosphor than with Nd^{3+} ions. The different energy transfer paths of $Cr^{3+} \rightarrow Ln^{3+}$ lead to different luminescence properties of the samples, which increases the potential of the phosphors for multifunctional applications. The NIR pc-LEDs prepared from phosphors **1–3** possess a good night vision and penetrating ability. Phosphors **2** and **3** have good application potential in c-Si solar cells. Furthermore, the SNGP:0.15Cr^{3+},0.03Nd^{3+},0.15Er^{3+} phosphor as a ratiometric luminescent thermometer exhibits a good relative sensitivity ($S_R > 1\%$) in the region from 340 to 588 K. The results suggest that the SNGP:Cr^{3+},Ln^{3+} NIR phosphors show satisfactory versatility.

Author contributions

This manuscript was written through contributions of all authors. All authors have given approval to the final version of the manuscript.

Conflicts of interest

The authors declare no competing financial interest.

Acknowledgements

This study was financially supported by the National Natural Science Foundation of China (grant no. 52072363), the special fund of Jiangsu Province for the transformation of scientific and technological achievements (BA2020007), the Key Research Program of the Chinese Academy of Sciences (grant no. ZDRW-CN-2021-3-3), and the Natural Science Foundation of Jilin province (20200201106JC).

References

1 R. Jiang, J. Yang, Y. Meng, D. Yan, C. Liu, C. Xu and Y. Liu, *Dalton Trans.*, 2020, **49**, 6074–6083.
2 Y. Zhang, S. Miao, Y. Liang, C. Liang, D. Chen, X. Shan, K. Sun and X. J. Wang, *Light: Sci. Appl.*, 2022, **11**, 136.
3 Z.-H. Zheng, B.-M. Liu, Z. Zhou, C.-G. Ma and J. Wang, *J. Mater. Chem. C*, 2022, **10**, 8797–8805.
4 J. Qin, J. Xiang, H. Suo, Y. Chen, Z. Zhang, X. Zhao, Y. Wu and C. Guo, *J. Mater. Chem. C*, 2019, **7**, 11903–11910.
5 S. Miao, Y. Liang, D. Chen, R. Shi, X. Shan, Y. Zhang, F. Xie and X. J. Wang, *ACS Appl. Mater. Interfaces*, 2022, **14**, 53101–53110.
6 X. H. Chen, E. H. Song, Y. Y. Zhou, F. Q. He, J. Q. Yang and Q. Y. Zhang, *J. Mater. Chem. C*, 2021, **9**, 13640–13646.
7 Q. Lin, Q. Wang, M. Liao, M. Xiong, X. Feng, X. Zhang, H. Dong, D. Zhu, F. Wu and Z. Mu, *ACS Appl. Mater. Interfaces*, 2021, **13**, 18274–18282.
8 H. Xiao, J. Zhang, L. Zhang, H. Wu, H. Wu, G. Pan, F. Liu and J. Zhang, *Adv. Opt. Mater.*, 2021, **9**, 2101134.
9 S. Fang, T. Lang, M. Cai and T. Han, *J. Alloys Compd.*, 2022, **902**, 163825.
10 K. Maciejewska, A. Bednarkiewicz and L. Marciniak, *Physica B*, 2021, **620**, 413247.
11 H. Zhang, J. Zhong, X. Zhang, H. Yang, Z. Mu and W. Zhao, *J. Alloys Compd.*, 2022, **894**, 162386.
12 K. Elzbieciak-Piecka, C. Matuszewska and L. Marciniak, *New J. Chem.*, 2019, **43**, 12614–12622.
13 W. Piotrowski, L. Dalipi, R. Szukiewicz, B. Fond, M. Dramicanin and L. Marciniak, *J. Mater. Chem. C*, 2021, **9**, 12671–12680.
14 L. Marciniak, A. Bednarkiewicz, J. Drabik, K. Trejgis and W. Strek, *Phys. Chem. Chem. Phys.*, 2017, **19**, 7343–7351.
15 W. M. Piotrowski, K. Maciejewska, L. Dalipi, B. Fond and L. Marciniak, *J. Alloys Compd.*, 2022, **923**, 166343.
16 L. Dong, J. Hou, B. Shao, S. Zhao and Y. Fang, *Opt. Mater.*, 2022, **127**, 112290.
17 P. Kumar, Kanika, S. Singh, R. Lahon, A. Gundimeda, G. Gupta and B. K. Gupta, *J. Lumin.*, 2018, **196**, 207–213.
18 P. K. Tawalare, V. B. Bhatkar, S. K. Omanwar and S. V. Moharil, *J. Alloys Compd.*, 2019, **790**, 1192–1200.
19 L. Dong, L. Zhang, Y. Jia, Y. Xu, S. Yin and H. You, *Ceram. Int.*, 2021, **47**, 3127–3135.
20 F. Fan, S. Yu, Y. Li, Y. Xu, Y. Song, Y. Yan, H. Wu, W. Wang and L. Zhao, *Inorg. Chem.*, 2022, **61**, 13618–13626.

 This journal is © The Royal Society of Chemistry 2023

Open Access Article. Published on 09 February 2023. Downloaded on 5/20/2025 11:15:26 PM.
This article is licensed under a Creative Commons Attribution 3.0 Unported Licence.

21 J. Zhong, Y. Zhuo, F. Du, H. Zhang, W. Zhao and J. Brgoch, *ACS Appl. Mater. Interfaces*, 2021, **13**, 31835–31842.
22 X. Xu, Q. Shao, L. Yao, Y. Dong and J. Jiang, *Chem. Eng. J.*, 2020, **383**, 123108.
23 P. Huang, W. Zheng, D. Tu, X. Shang, M. Zhang, R. Li, J. Xu, Y. Liu and X. Chen, *Adv. Sci.*, 2019, **6**, 1802282.
24 D. Huang, Q. Ouyang, H. Xiao, B. Wang, H. Lian, Q. Zeng and J. Lin, *Dalton Trans.*, 2021, **50**, 908–916.
25 F. Zhao, Z. Song and Q. Liu, *Laser Photonics Rev.*, 2022, **16**, 2200380.
26 G. Liu, M. S. Molokeev and Z. Xia, *Chem. Mater.*, 2022, **34**, 1376–1384.
27 G. Wei, P. Li, R. Li, J. Li, Y. Shi, Y. Wang, S. He, Y. Yang, H. Suo and Z. Wang, *Inorg. Chem.*, 2022, **61**, 5665–5671.
28 X. Zou, H. Zhang, W. Li, M. Zheng, M. S. Molokeev, Z. Xia, Y. Zheng, Q. Li, Y. Liu, X. Zhang and B. Lei, *Adv. Opt. Mater.*, 2022, **10**, 2200882.
29 X. Luo, X. Yang and S. Xiao, *Mater. Res. Bull.*, 2018, **101**, 73–82.
30 L. Yao, Q. Shao, S. Han, C. Liang, J. He and J. Jiang, *Chem. Mater.*, 2020, **32**, 2430–2439.
31 L. Zhang, L. Dong, B. Shao, S. Zhao and H. You, *Dalton Trans.*, 2019, **48**, 11460–11468.
32 J. Zhu, Z. Xia and Q. Liu, *Mater. Res. Bull.*, 2016, **74**, 9–14.
33 Y. Jin, Z. Zhou, R. Ran, S. Tan, Y. Liu, J. Zheng, G. Xiang, L. Ma and X. J. Wang, *Adv. Opt. Mater.*, 2022, **10**, 2202049.
34 C. Yuan, R. Li, Y. Liu, L. Zhang, J. Zhang, G. Leniec, P. Sun, Z. Liu, Z. Luo, R. Dong and J. Jiang, *Laser Photonics Rev.*, 2021, **15**, 2100227.
35 Z. Jia, C. Yuan, Y. Liu, X. J. Wang, P. Sun, L. Wang, H. Jiang and J. Jiang, *Light: Sci. Appl.*, 2020, **9**, 86.
36 F. Zhao, H. Cai, Z. Song and Q. Liu, *Chem. Mater.*, 2021, **33**, 3621–3630.
37 F. Zhao, H. Cai, Z. Song and Q. Liu, *Chem. Mater.*, 2021, **33**, 8360–8366.
38 Q. Zhang, X. Wang and Y. Wang, *J. Alloys Compd.*, 2021, **886**, 161217.
39 C. Zhong, L. Zhang, Y. Xu, X. Wu, S. Yin, X. Zhang and H. You, *Mater. Today Chem.*, 2022, **26**, 101233.
40 C. Zhong, L. Zhang, Y. Xu, X. Wu, S. Yin, X. Zhang and H. You, *J. Alloys Compd.*, 2022, **903**, 163945.
41 L. Kong, Y. Liu, L. Dong, L. Zhang, L. Qiao, W. Wang and H. You, *Dalton Trans.*, 2020, **49**, 8791–8798.
42 F. Du, Y. Nakai, T. Tsuboi, Y. Huang and H. J. Seo, *J. Mater. Chem.*, 2011, **21**, 4669.
43 L. Dong, L. Zhang, Y. Jia, Y. Xu, S. Yin and H. You, *Inorg. Chem.*, 2020, **59**, 15969–15976.
44 Y. Zhong, S. Gai, M. Xia, S. Gu, Y. Zhang, X. Wu, J. Wang, N. Zhou and Z. Zhou, *Chem. Eng. J.*, 2019, **374**, 381–391.
45 S. Liang, G. Li, P. Dang, Y. Wei, H. Lian and J. Lin, *Adv. Opt. Mater.*, 2019, **7**, 1900093.
46 Y. Chen, J. He, X. Zhang, M. Rong, Z. Xia, J. Wang and Z. Q. Liu, *Inorg. Chem.*, 2020, **59**, 1383–1392.